ELSEVIER

Nuclear Instruments and Methods in Physics Research A 432 (1999) 24–47

NUCLEAR INSTRUMENTS & METHODS IN PHYSICS RESEARCH Section A

www.elsevier.nl/locate/nima

Simulation and measurement of the fringe field of the 1.5 T BABAR solenoid

E. Antokhin[a], A. Buzykaev[a], A. Chupyra[a], D. Fedorov[a], S. Ganzhur[a], G. Kolachev[a], A. Litvinov[a], A. Medvedko[a], V. Mikerov[a], S. Mikhailov[a], A. Onuchin[a], Sh. Singatulin[a], R. Aleksan[b], Ph. Bourgeois[b], L. Gosset[b], P. Graffin[b], G. London[b,*], J.-Ph. Mols[b], J.-Ch. Toussaint[b], M. Berndt[c], R. Coombes[c], S. Ecklund[c], D. Jensen[c], L. Keller[c], J. Krebs[c], H. Lynch[c], Z. Wolf[c]

[a]*Budker Institute of Nuclear Physics, Novosibirsk, Russia*
[b]*CEA, DAPNIA,CE-Saclay, F-91191 Gif-sur-Yvette, France*
[c]*Stanford Linear Accelerator Center, P.O.Box 4349, Stanford, CA 94309, USA*

Received 12 November 1998; received in revised form 5 March 1999

Abstract

In the context of the SLAC PEP-II asymmetric e^+e^- collider and the BABAR detector with its 1.5 T solenoid, we have calculated and measured the fringe field at the nearby beam elements and at the position of the photomultipliers external to the return iron but within a specially designed iron shield. The comparisons of these measurements with the simulations based on finite element analysis are remarkably good, within about 5 G at the most critical beam element. The field at the photomultipliers is less than 1 G, in agreement with the simulation. With a simple method of demagnetization of the shield, a maximum field of 0.6 G is obtained.

Keywords: Magnetic shielding; Measurements of magnetic fields; Finite element analysis; B-factory experiment; CP-violation

1. Introduction

1.1. CP-*violation*: *PEP-II and* BABAR

The study of B^0 decays and the resulting CP-violating asymmetries will test our understanding of the Standard Model. The SLAC PEP-II asymmetric e^+e^- collider [1] (9 GeV electrons interacting with 3.1 GeV positrons), now under construction, will produce the $\Upsilon(4S)$ state with a $\beta\gamma = 0.56$. The boost of the decaying B^0 in the laboratory enables the measurement of the time order of the B^0-$\bar{B}^0$ pairs, crucial to detect CP-violation.

The BABAR detector [2] will surround the interaction point (IP) in an asymmetric way to allow more flight path for the particles in the electron direction; the offset is 370 mm. In order to maximize the luminosity, the machine elements must be very close to this interaction point; therefore BABAR and the last elements are very close to each other.

* Corresponding author. Tel.: 33-1-690-86156; fax: 33-1-690-86428.

E-mail address: london@hep.saclay.cea.fr (G. London)

0168-9002/99/$ - see front matter
PII: S0168-9002(99)00278-8

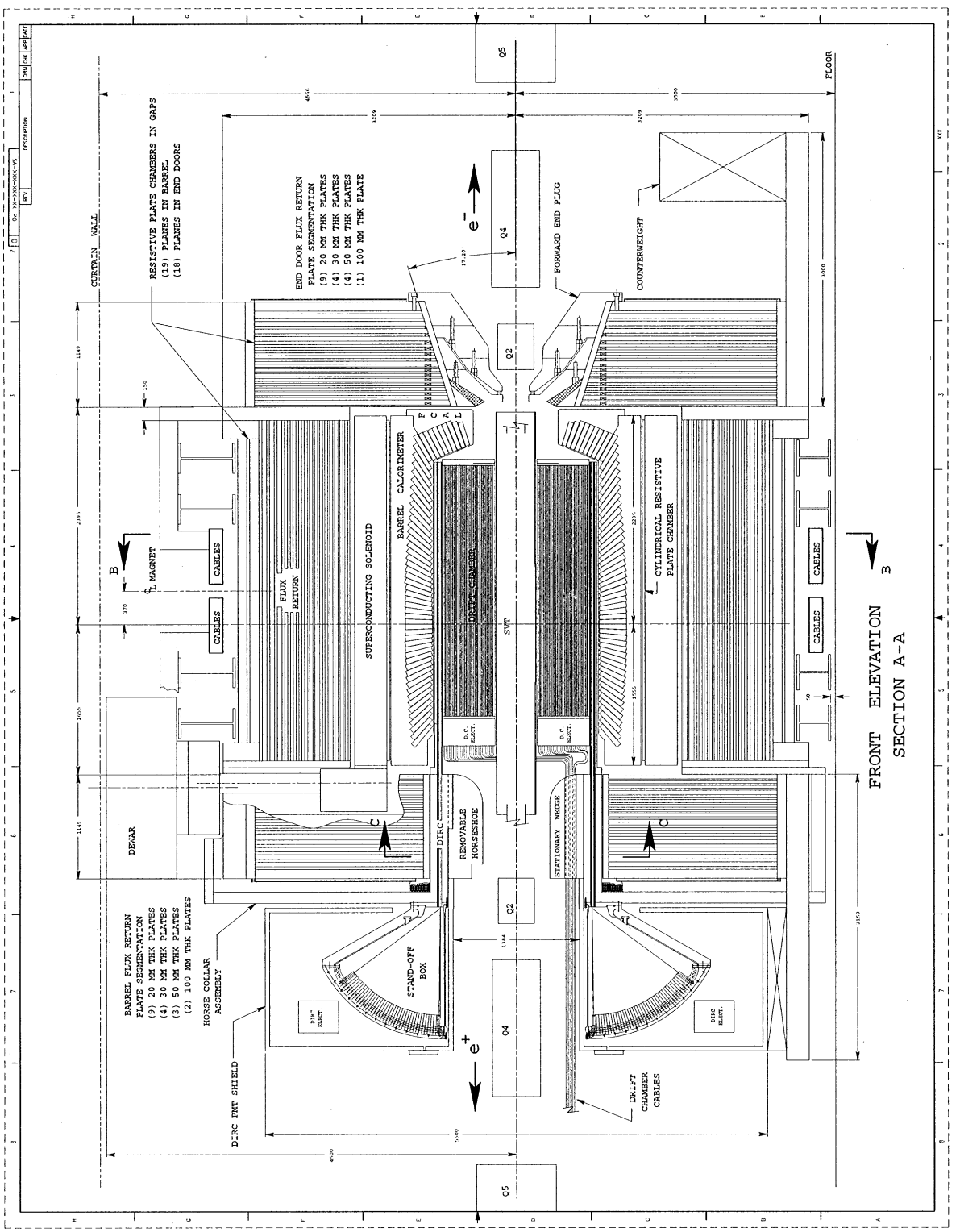

Fig. 1. Side view of BABAR. The magnet right-handed coordinate system is given by the e^- = + Z direction and the vertical direction = + Y with the origin at the center of the magnet.

The detector, which is under construction, consists of a 1.5 T solenoid with an iron flux return in the form of a barrel closed by two end caps, consisting of two doors each, in addition to a number of sub-detector elements, namely from the IP radially out, the Silicon Vertex Tracker, Drift Chamber, DIRC (Detector of Internally Reflected Cherenkov light), CsI Calorimeter and Instrumented Flux Return for Muon Detection. It is shown in Fig. 1 with the nearby machine elements, and schematically in Fig. 2 which emphasizes the magnetic elements. Since the elements are symmetric about the interaction point, their relationship to the detector is quite different in the two directions; for example, notice the position of Q2 with respect to the flux return.

Notice also that since the detector and machine elements are in close proximity, the final elements are in a very strong fringe field. This field could degrade the performance of the quadrupoles, reducing the luminosity significantly and the possibility to detect CP-violation.

1.2. DIRC

The DIRC [3] is the principal particle identification system of BABAR. It consists of quartz bars inside the detector and of a large pure water tank (the Standoff Box) supporting photomultipliers outside the detector. The quartz bars and the Standoff Box are supported by a complex mechanical structure which is attached to the outside of the barrel iron via an external support structure (ESS) composed of a structural element in the form of a "horsecollar" and a gusset plate.

Charged particles, produced at the interaction point inside the detector, traverse the quartz bars in which Cherenkov radiation is produced. The angle of this radiation with respect to the incident particles is a measure of the speed of these particles. The Cherenkov photons are propagated along the length of the rectilinear bars by total internal reflection, preserving the angular information and exiting outside the detector into the Standoff Box. This water tank is composed of a cylinder, cone and 12 sectors which are cylindrical sections. The photomultipliers are mounted on the sectors placed at about 1.17 m from the exit point to permit a precise measurement of the angle for each photon. The tubes are arranged in a closely packed array to maximize the number of detected photons, and light catchers are added to increase the effective

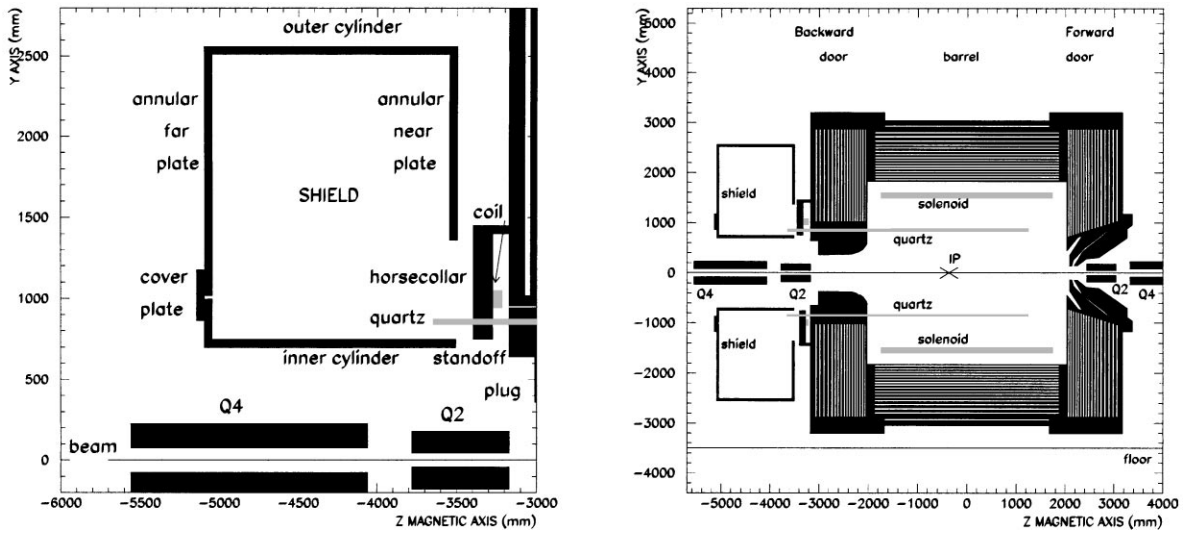

Fig. 2. Schematic side view of the active and passive magnetic elements of the BABAR detector and nearby PEP-II machine elements, with a zoom on the shield concept. The quartz is included to indicate the reason for the big gap in the magnetic circuit. IP denotes the interaction point.

solid angle for photon detection. The Cherenkov process is a weak source of photons which will be detected in the single-photon counting mode.

The Q2 quadrupoles and the 10 752 photomultipliers reside outside the main iron flux return but in the considerable fringe field of the 1.5 T solenoid magnet. In conjunction with a bucking coil in the backward direction, which is necessary to reduce the B_Z field at Q2 to less than about 100 G, a magnetic shield surrounding the Standoff Box has been studied which reduces the fringe field at the photomultipliers to an acceptable level, less than 1 G. The field in the shield iron should be less than 0.1 T everywhere, though it might attain 0.8 T in some places in case of malfunctioning of the bucking coil or solenoid; a de-magnetization scheme must be envisioned.

1.3. Scope of article

In this article, we shall only consider the fringe field in the backward direction as it affects the quadrupoles, namely Q2, and the DIRC photomultipliers.

We shall define the fringe field requirements in Section 2, describe the simulation of the field in Section 3, present the design and construction of the shield in Section 4 and define the bucking coil in Section 5. The mappers of the DIRC in Section 6 and quadrupole in Section 7 regions are then described. After presenting the results of the measurements in Section 8, we conclude in Section 9.

2. PMT and Q2 requirements from measurements

Measurements were made to determine the performance of the PMTs and the quadrupoles in a magnetic field, resulting in target limits.

2.1. PMT performance in a magnetic field

The PMT used in the DIRC is the Thorn-EMI 9125FLB. It has a 28.2 mm diameter and a bialkali photocathode with a high blue response. It is well suited for our single-photon counting requirement. The dynodes are rectangular and thus the effects of a transverse magnetic field will depend on the orientation.

It has been tested with a pulsed blue light at a wavelength of 450 nm in magnetic fields up to 20 G, measured with an accuracy of 0.2 G [4]. The orientations of the field relative to the tube were longitudinal and transverse, with the latter in the two directions: across the dynode ("favorable") and along the dynode ("unfavorable"). The PMT was operated at a high voltage such that the single-photon peak was at 20 mV, i.e. as we shall run in BABAR. For a 95% efficiency, i.e. we lose 1/20 of the photoelectrons, the acceptable transverse field is about ± 3 (1) G in the favorable (unfavorable) direction, with about a 0.5 G asymmetry. The principal reason for the inefficiency is due to the perturbation of the electron multiplication, i.e. gain reduction, in the unfavorable orientation, and the decrease in the efficiency of photoelectron collection in the favorable orientation. The acceptable longitudinal field giving 95% efficiency is about 3 G, also asymmetric about 0, with the efficiency falling more slowly than in the transverse direction.

From these measurements, we concluded that we would orient the PMTs transversely so that the anticipated lower field component, azimuthal with respect to the solenoid axis, is in the unfavorable transverse direction.

2.2. Quadrupole performance in a magnetic field

The major effect of the approximately axial solenoid fringe field on the quadrupoles is to induce higher-order multipoles, in particular a skew octupole, due to flux concentration on the poles of the quadrupole. Beam studies have indicated that the multipole requirement is $\leq 10^{-4}$ for $n = 3$–15 [5].

We will concentrate on the Q2 quadrupole since it is most affected by the solenoid fringe field. This water-cooled laminated iron quadrupole must accomodate both the high-energy (HEB) and low-energy rings (LEB), as seen in Fig. 3. It is slightly offset, and therefore has a dipole component as well. The LEB part has inner bore radius of 47.8 mm, and a length of 610 mm. The maximum design current is 1100 A on 8 turns, with a current density

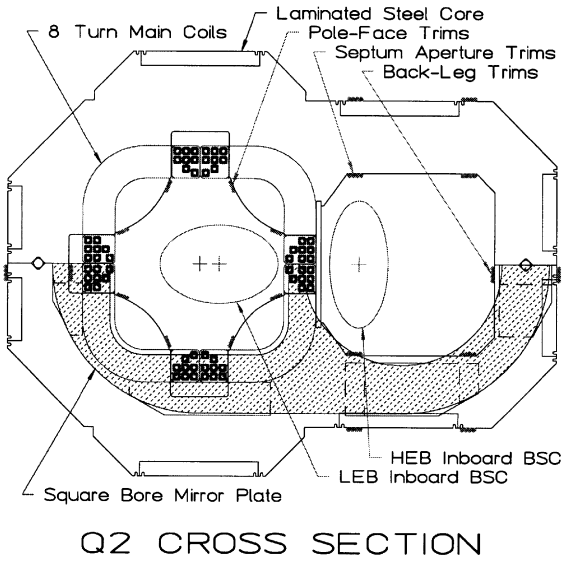

Fig. 3. Schematic cross section for Q2. The LEB is off-set as it goes through the quadrupole on the left, while the HEB is in a "field-free" region, as shown on the right. The "beam-stay-clear" (BSC) regions are indicated. Only one half of the Mirror Plate is shown.

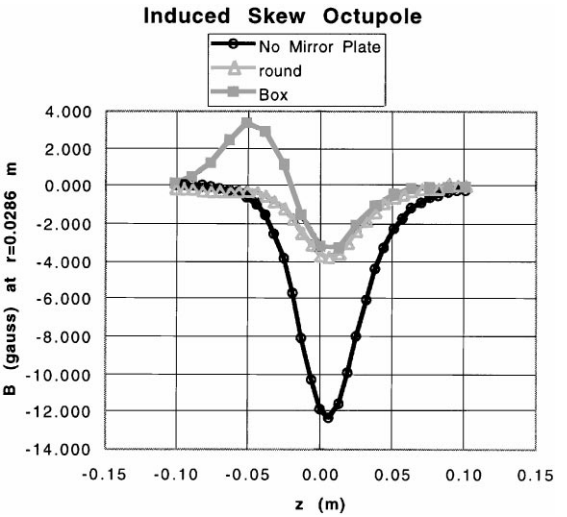

Fig. 4. Skew-octupole vs. Z for different mirror plate configurations.

of 57 A/mm^2. There are trim windings to cancel or reduce the $n = 3$ term in the main quadrupole field, to buck the solenoid-induced dipole and skew octupole.

In order to reduce the induced octuple, the quadrupole has a mirror plate on the IP side, connected magnetically to the quadrupole iron. The opening in the mirror plate is 96.6 mm square with rounded corners. The plate is 9.5 mm thick and is placed at 38 mm from the main quadrupole iron, connected at the outer radius. The solenoid field induces a skew octupole in the mirror plate of opposite sign to that induced in the quadrupole body providing cancellation due to the 45° rotation of the mirror plate relative to the quadrupole iron.

An analytical calculation gives for the induced octupole: $\int_{Z_0}^{\infty} a_4(Z)\,\mathrm{d}Z = (\alpha/4)\bar{B}_Z R_\mathrm{i}$ where Z_0 the offset from the pole face ($= R_\mathrm{i}/4$), α the linkage coefficient $= 0.4$–0.8 depending on the chamfer, $\bar{B}_Z$ is the average axial field integrated over the same limits, and R_i is the inner bore radius.

Harmonic measurements were made with a thin air-core solenoid placed at 170 mm from the core-edge of a Q2 model, which had the possibility to include mirror plates of varying shapes. The field was 360 G at the center of the solenoid, 216 G at the mirror plate and 71 G at the core-edge. The skew octupole was measured between ± 100 mm with respect to the Q2 core-edge. The results without a mirror plate are shown in Fig. 4, as well as those for two different shapes: annular and box opening. Without a mirror plate, the value was always negative, with a peak at the core-edge. With mirror plate, the value changed sign at the core-edge, with the integral closest to 0 for the box variation. The latter was adopted for the definitive design. (Annular mirror plates are used at both ends for Q4.)

3. Simulation with BABAR model

3.1. BABAR *magnetic circuit*

The BABAR magnetic circuit consists of two active elements: a thin 1.5 T cryogenic solenoid and a bucking coil in the backward direction. The mean radius of the solenoid is 1532 mm while its length is 3456 mm. The bucking coil is a warm magnet which can operate at ± 1.5 times the expected operating current (see Section 5).

Its passive elements consist of a barrel, forward and backward endcaps and plugs, part of the DIRC support structure (the Strong Support Tube, or SST, radially between the backward door and the plug, and the ESS connection to the barrel iron) and the DIRC shield. The quadrupoles need to be treated as passive elements only. The ensemble of the elements is extremely complicated from a magnetic point of view, even for the axisymmetric approximation. This is mainly due to the varying thicknesses of the thin plates and narrow gaps which make up the instrumented flux return in the barrel and door regions (see Fig. 5). The other area of complication comes from the plugs which need careful shaping to obtain the uniform field requirements inside the drift chamber fiducial volume and to prevent too large of a leakage towards the quadrupoles especially in the forward direction. In the backward plug region, the DIRC support structure is part of the magnetic circuit, but the fragile quartz bars and bar boxes require holes in this part of the circuit, increasing the fringe field in the backward direction in a significant way (see Fig. 6). Note that the horsecollar is magnetically connected to the door iron; this is an approximation for the part which is not axisymmetric.

In addition, there are the inevitable non-axisymmetric passive elements: the drift chamber cable holes in the backward plug, the upwards chimney passage for the cryogenics services, the skid plates under the two doors (to allow opening for access), the ESS, the quadrupoles and some smaller features.

However, some of these elements have a left–right symmetry, making the analysis somewhat simpler. In addition, while the hexagonal shape of the barrel and door iron is not strictly axisymmetric, that approximation turns out to be a good one.

3.2. 2D with Castem 2000 and Mermaid

In order to satisfy the PMT and Q2 requirements, it was recognized early that a combination of active (bucking coil) and passive elements (iron) was necessary.

There are external constraints on the shielding arrangement. They include:

- The shield is most strongly determined by the Standoff Box which is shown in Fig. 7, cantilevered from the horsecollar. Part of the shield must consist of an inner cylinder at a radius inferior to that of the Standoff Box.
- Beam elements will be contained within the shield cylinder. They are supported in cantilever, limiting the length of the shield along Z, i.e. $\geq$ about -5000 mm. The radial extent of the beam elements is determined by seismic considerations, and vary as a function of Z. The shield cylinder is thus sandwiched between these beam elements and the Standoff Box.
- Access to the drift chamber is made inside the shield cylinder. This access is quite difficult because the beam elements fill a large fraction of the relatively small radial dimensions. However, only the upper part of the shield cylinder can be removed without moving the beam elements.
- Access to other parts of the detector requires that the BABAR doors open laterally on the moveable skid plates. The shield should also open laterally for Standoff Box access. Since the opened BABAR doors are no longer bolted to the barrel iron, they are quite unstable due to their aspect ratio; therefore counterweights are required on the skid plates. Given the small radial space between the Standoff Box and the skid plates, there is little room for a dedicated counterweight. Thus the magnetic shield and its support, resting on the skid plates, should also provide a counterweight for the BABAR doors, when opened.
- The shield should provide a stop for the backward plug against movements in the $-Z$ direction due to a seismic event.

Studies were performed initially using Castem 2000[1] and subsequently with Mermaid.[2] The comparison of the results of the two codes using the same geometry and magnetic properties was very good. The 2D results of Castem 2000 are presented since the code allows the use of more than three different regions with variable permeability.

[1] The Castem 2000 code was developed in the Saclay laboratory [6].

[2] The Mermaid code was developed in the Budker Institute [7].

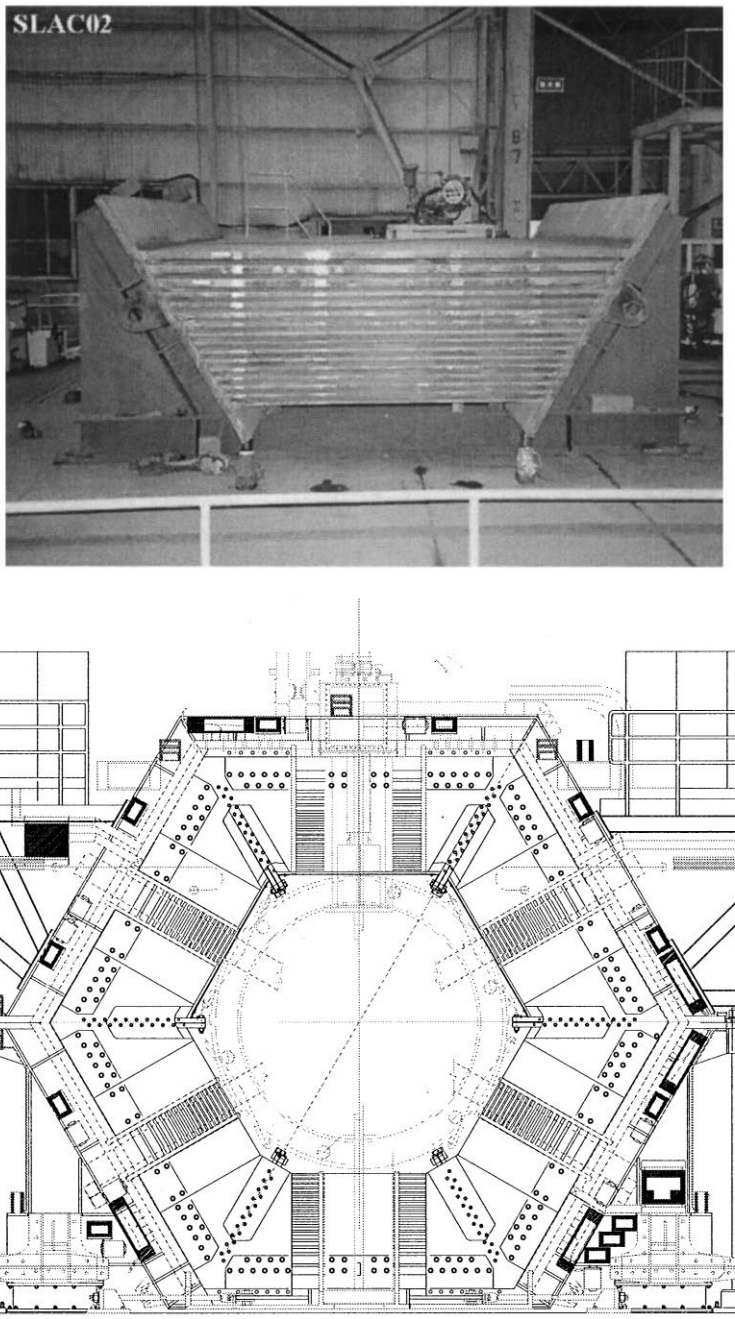

Fig. 5. The BABAR iron: one of six barrel sectors of the instrumented flux return in construction, and end view design of barrel viewed from back.

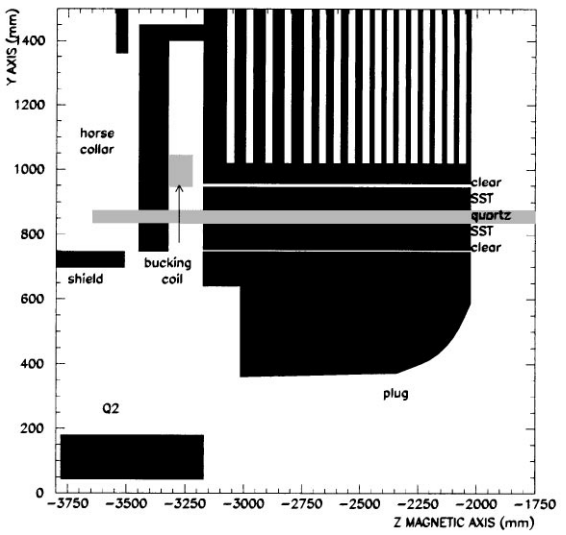

Fig. 6. The BABAR iron: schematic details of the backward region, including the bottom part of door, the plug, SST and horsecollar. The quartz is included to indicate the reason for the big gap in the magnetic circuit.

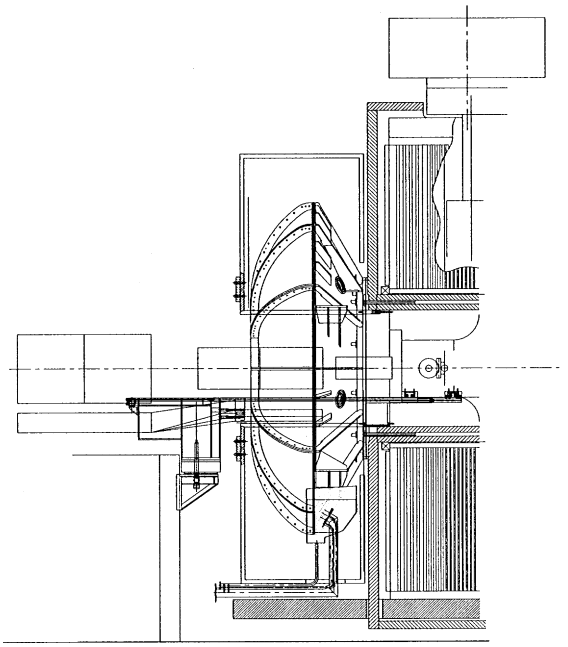

Fig. 7. Side view of the DIRC Standoff Box and shield, with BABAR iron. The Standoff Box is cantilevered from the horsecollar which is connected to the BABAR iron, while the shield is supported by the skid plate which also supports the BABAR backward doors.

The PMT closest to the beam line is more sensitive to the bucking coil current than the furthest PMT. In general, at the optimum bucking coil current, the maximum transverse field at the PMTs occurred at these two extremes, but with opposite sign. An iterative series of studies were made minimizing the maximum transverse field at the photomultipliers at the optimum bucking coil current. The studies concerned:

- The position of the bucking coil: to be most effective in compensating the flux leakage, the bucking coil was placed at the exit of the hole for the quartz.
- The range of magnetic field for which the iron needed a high permeability: see Fig. 8 where the maximum field needed for the shield studies is $H = 100$ A/m.
- The thickness of the iron: the influence of the thickness of the iron shield varied little between 40 and 60 mm and was chosen to be 50 mm.
- The magnetic gap between the shield iron and the plug/SST was found necessary but not very sensistive beyond a minimum distance.
- The dimensions of the horsecollar were increased to provide a path for the magnetic flux which avoided the inside of the shield.
- The shape of the shield iron was varied between closely following the Standoff Box and a cylindrical shape, easier to fabricate; the result was quite insensitive to this choice.
- The point at which the shield inner cylinder should connect to the remaining part of the shield was the closest to the null point at which the field changes sign. This latter point is quite delicate in that it is quite close to the PMTs closest to the beam line.

These studies resulted in a concept (see Fig. 2) with an inner cylindrical shell and an outer structure split in halves. The two halves consist of an outer cylindrical shell, two annular end-plates ("near" and "far"), an annular cover plate, support structures, and braces to the back door. The inner cylindrical shell is divided longitudinally into a fixed lower part (about 1/3) and a moveable upper part (about 2/3). The fixed part is connected to a standoff shell in cantilever from the backward plug.

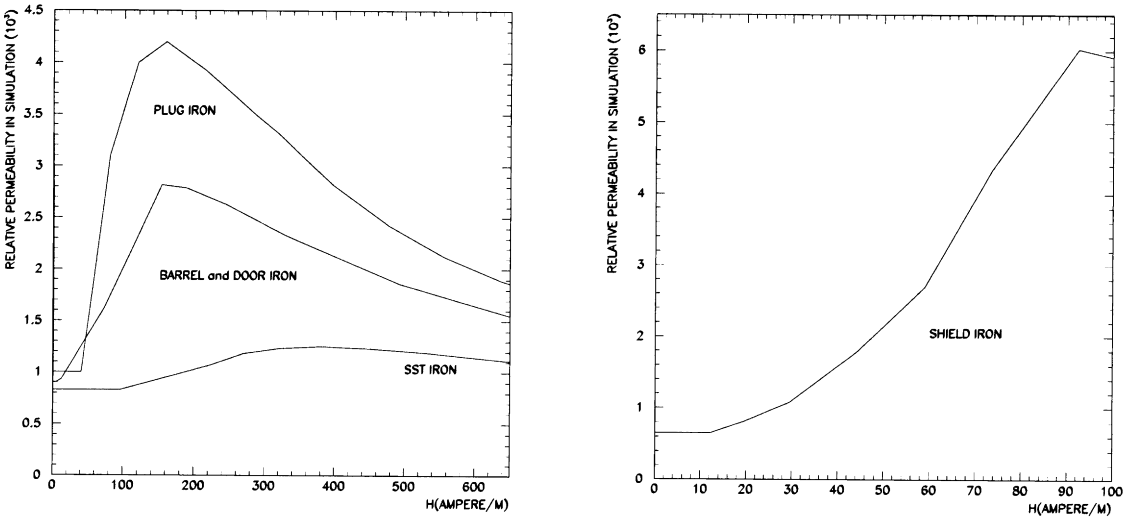

Fig. 8. Magnetic properties assumed for different materials in the simulation. The left figure is for barrel, door, plug and SST iron, while the right figure is for the shield iron. Note the different scales, in particular the abscissa.

For the shield design parameters, the simulation showed that, at the optimum bucking coil current for the PMTs, about 30.7 kA-turns, the transverse magnetic field at the PMTs is about 0.2 G as seen in Fig. 9. The optimum bucking coil current for Q2 is higher by about 15%, requiring a compromise. Since the optimization was done in 2D, the value of the current is only approximate; however the relative optima for the PMTs and Q2 should be verified.

The flux lines near the DIRC shield are shown in the same figure. Notice the influence of the horse-collar and the mirror plate of Q2, as well as the magnetic opening for the quartz and the cover plates. The reversal of the flux direction in the annular far plate is related to the zero in $B_{\perp}$ observed in the upper curve.

3.3. 3D with Mermaid

Three-dimensional studies were made to study the effects of the different non-axisymmetric aspects of the BABAR iron [9]. In addition, they permitted an evaluation of the gaps between the two shield halves, necessary at the top for cable access, and at the bottom for water pipe access. The Mermaid 3D computer code was used for this purpose. This code allows us to have a mesh for calculations with up to 2×10^6 nodes at Pentium computer with 128 Mb memory core.

3.3.1. *Simple axisymmetric version of* BABAR

Before starting 3D calculations, we compared the results using the Mermaid 2D code with those obtained by Mermaid 3D for exactly the same axisymmetrical geometry. The comparison was performed in two regions of interest: inside the shield at the PMTs location and near Q2. The difference does not exceed 0.2 G for the PMT region and 5 G for the Q2 region. This accuracy could be improved by a finer meshing.

Due to the complexity of the BABAR magnetic circuit, it was not possible to make a 360° model within the memory limitations. Therefore, we considered two models with either left–right or top–bottom symmetry.

3.3.2. *Left–right and top–bottom symmetric models of* BABAR

In Fig. 10, one sees the BABAR model with left–right symmetry. It was used to study the effects

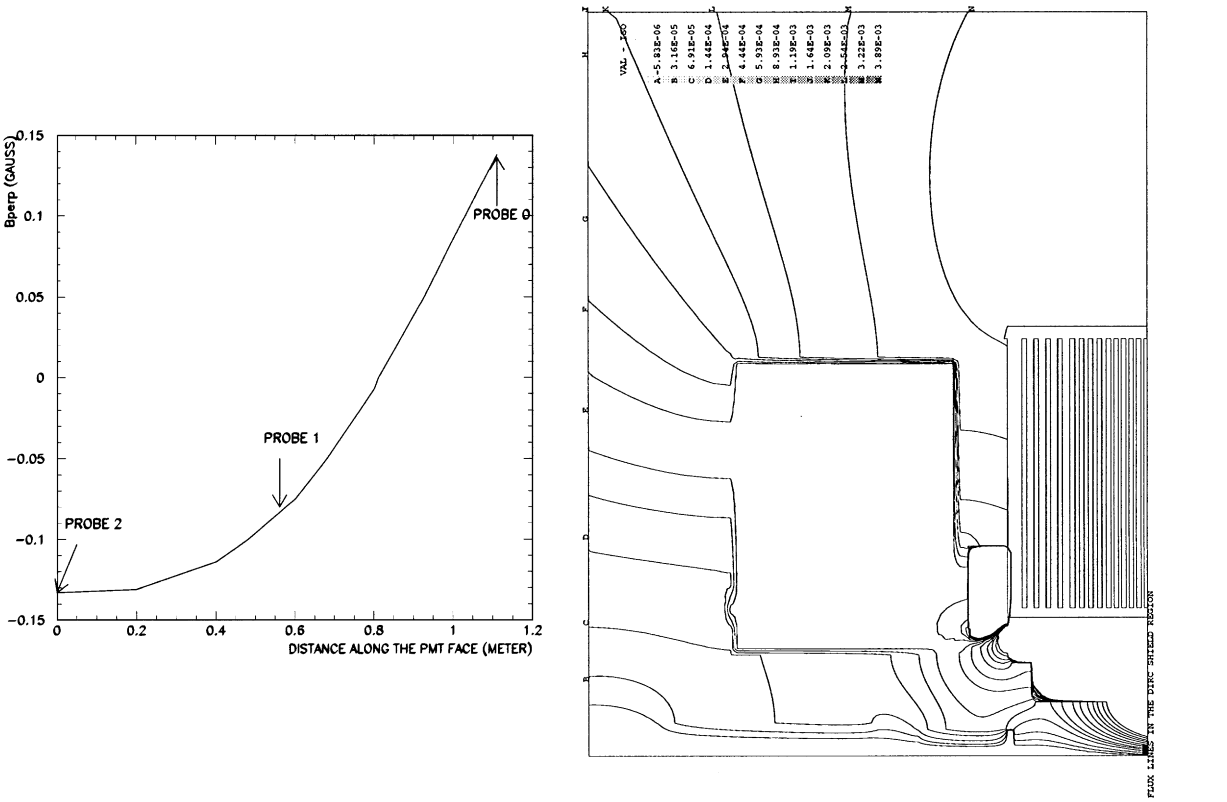

Fig. 9. Results of the 2D modelization of *BABAR* using the measured permeability (see Section 4). The figure on the left gives the $B_\perp$ along PMT face from probe 2 to probe 0 (see Section 6) while the figure on the right gives the flux lines in the DIRC shield region.

of the top–bottom asymmetries, in particular

- the chimney for the cryogenics at the top,
- the cable holes in the bottom of the plug,
- non-symmetrical 5 mm split between the removable and fixed parts of the backward plug,
- the skid plate on the bottom.

By using extreme values for the parameters, we have determined that the major effect is due to the ESS and the chimney cutout, i.e. the angular distribution reflects the angular variation of the magnetic reluctance between the near annular plate of the shield and the horsecollar. On the other hand, the angular variations due to the cable holes, split between removable and fixed parts of the plug, and skid plates are very small. The $B_\perp$ for this model varies between 0.3 and 0.7 G as seen in Fig. 11.

A BABAR model with top–bottom symmetry was used to study the effects of the left–right asymmetries, in particular Q2. Another left–right asymmetry was introduced to reflect an error in the mounting of the BABAR doors which produced an additional x-displacement of 7 mm. The model shows that the angular variations due to the Q2 asymmetry and the shift of one door are negligible [9].

Therefore, the results of the 3D simulations show that the expected $B_\perp$ inside the DIRC shield is less than 1 G with angular variations of about ± 0.2 G. Since a possible residual field (see next section) was not included in the model, the measured azimuthal dependence can be different in detail from the prediction.

3.4. Necessity of demagnetization

The calculations by Castem 2000 and Mermaid show that in the case of the crash of the main solenoid or bucking coil, the field in the shield iron

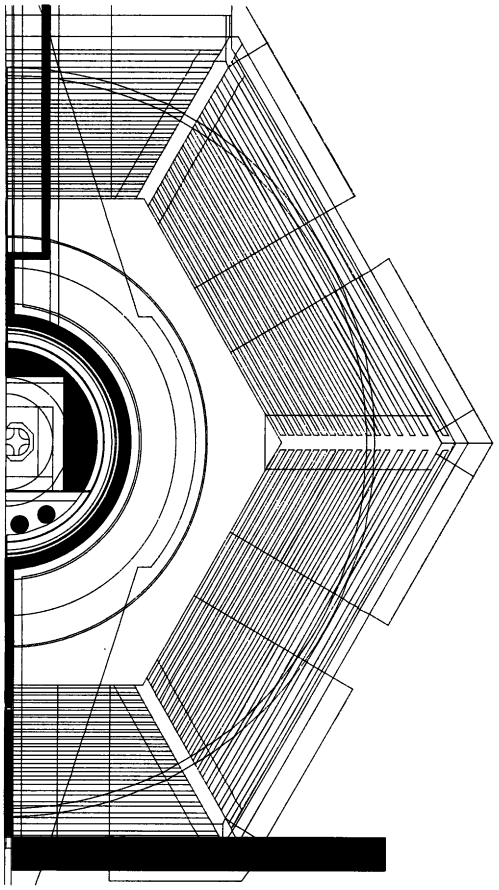

Fig. 10. Cross-section of left–right symmetry model of BABAR. Note the shape of the horsecollar. The up-down asymmetric elements are in black.

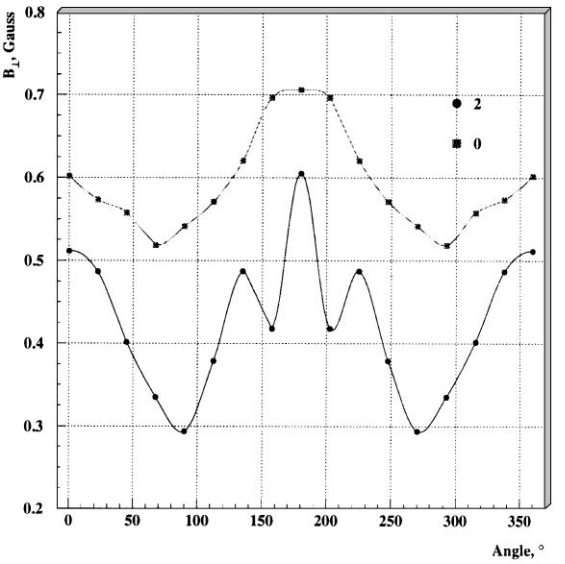

Fig. 11. $B_\perp$ vs. azimuthal angle calculated in the left–right symmetry model of BABAR. The coordinate system has the downward direction at 0°.

can reach 7 kG instead of 0.5 kG when both coils are on. The resulting coercive force is about 1 Oe for the very pure iron used in the shield construction. Therefore, the residual field of the iron could give an additional contribution to the fringe field in the PMTs region.

We estimated the residual field distribution inside the shield, simulating the magnetization of the iron by a coil applied to the shield iron from both inner and outer sides all along the contour of the shield. This coil inducing the magnetization field inside the iron should have a linear current density along the contour equal to the coercive force taken in A/cm. We assumed $j = 0.8$ A/cm corresponding to the value of the coercive force $H_c = 1$ Oe. The polarity of the current in the coil corresponded to the direction of the residual flux in the shield iron. This direction was taken from the calculation of the field at zero bucking coil current.

The value of the maximum perpendicular component at the PMTs, practically equal to the module of the field, reaches about 3 G on the upper PMTs and about 2 G on the lower PMTs. In this model, the residual field due to the coercive force exceeded the expected fringe field inside the shield. This led to a special effort to produce a shield with as small a coercive forces as possible, and to the consideration of the use of the bucking coil to demagnetize the shield. In this method, the amplitude of AC component of the bucking coil current should gradually decrease, for example (Fig. 12):

$$I^{\mathrm{BC}} = I_0^{\mathrm{BC}} + I_A^{\mathrm{BC}} \mathrm{Sin}\left(\frac{2\pi}{T_1}t\right) \mathrm{e}^{-t/T_2}, \quad T_1 \ll T_2.$$

Two different cases of the shield magnetization, due to main solenoid or bucking coil crashes, lead to two types of procedures. In the case when the main field cut, the demagnetization procedure has to have $I_0^{\mathrm{BC}} = 0$, while $I_0^{\mathrm{BC}} = I_{\mathrm{opt}}^{\mathrm{BC}}$ for the other case.

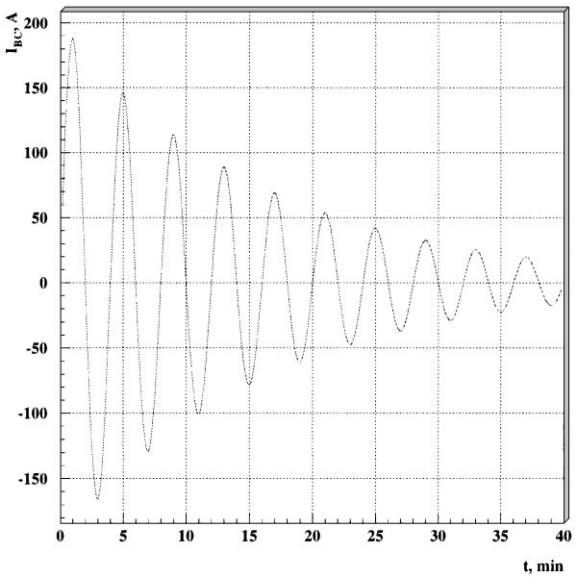

Fig. 12. Possible demagnetization procedure for the shield.

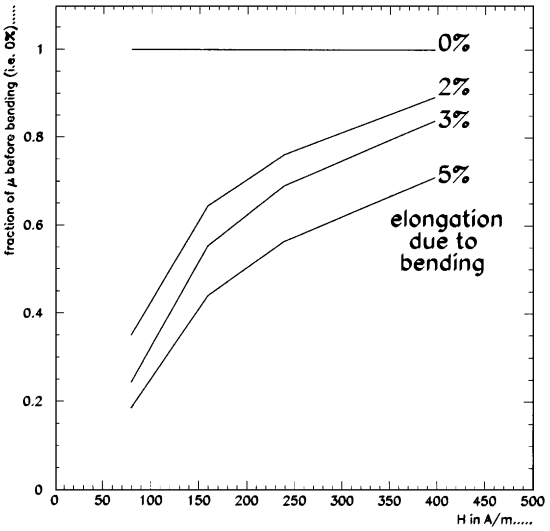

Fig. 13. Measurements of the deterioration of the permeability at low fields due to bending. The region which is relevant for our studies is $H \leq 100$ A/m. The inner cylinder corresponds approximately to the 2% curve. Scaling by the radii, the outer cylinder corresponds approximately to 0.5%.

To estimate T_1, we have to take into account that the skin depth has to be at least half of the shield thickness:

$$T_1 = \frac{\pi\mu\delta^2}{\rho} \approx 20 \text{ s},$$

for $\rho = 0.11$ μHom/m and average $\mu = 1000$.

About 10 cycles of bucking coil current would be enough to decrease the residual fields in a reasonable time.

4. Design and construction of the shield

The design of the shield was based on the following considerations:

- The outer part of the shield is cylindrical to minimize the number of elements to be connected.
- All connections are welded including the support structure, except for the cover plate to allow the opening of the shield doors and access to the Drift Chamber, and the flange on the fixed part of the inner cylinder to allow the opening of the Standoff Box.
- Since the necessary bending strongly affects the permeability, especially at low H (see Fig. 13 for measurement on a similar type of iron [8]), the entire structure must be annealed after construction. The manufacturer studied two cases: annealing at 550°C for 2 h and at 850°C for 4 h. The latter gave better results.
- The shield structure is welded to the skid plate at the bottom, and is welded to the BABAR door at the top via braces to prevent movement during a seismic event.

The construction of the shield with its special ultra low carbon steel was the responsibility of Kawasaki Heavy Industries (KHI). The material was EFE material, manufactured at Kawasaki Steel Corporation (KSC). The permeability and coercive force were measured at the manufacturer (see Figs. 14 and 15).These values were better than specifications in general. In particular, the measured permeabilities were better than that used in the original simulation (the right part of Fig. 8) leading to a reduction of 1.5 in the maximum $B_\perp$ expected. The measured coercive forces were about one half that assumed in the calculation of

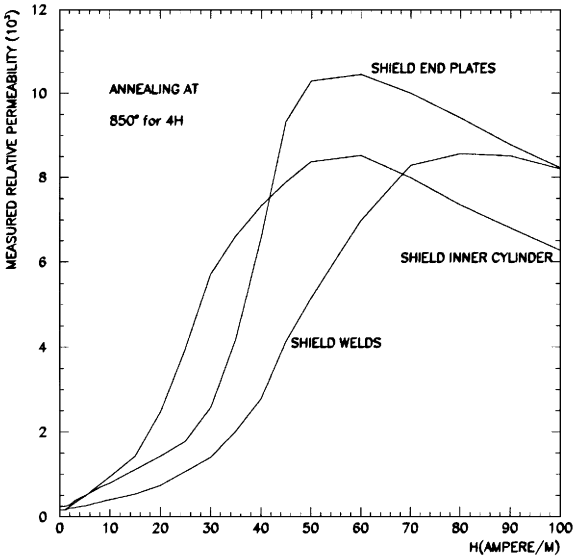

Fig. 14. Relative permeability vs. field for the shield material as measured at KSC.

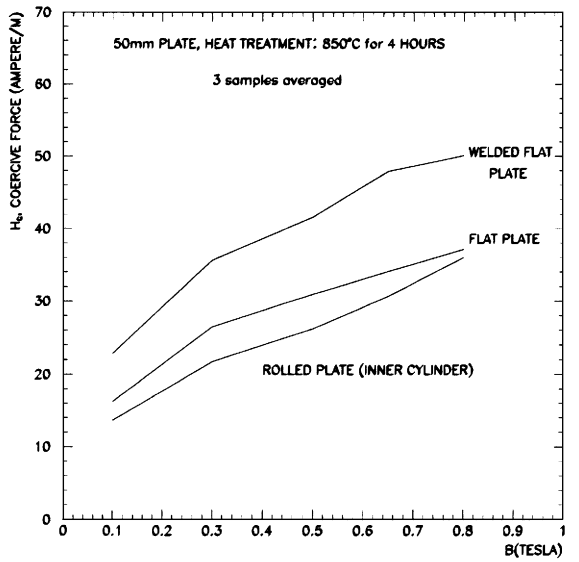

Fig. 15. Coercive force vs. field for the shield material as measured at KSC.

3.3; therefore the expected residual field should not exceed about 1.5 G.

The design of the Saclay laboratory is shown in Fig. 16. The cover plate is made in four pieces to facilitate the opening of the shield. The turn buckles take up the construction tolerances and are made rigid to provide a "stop" for the upper part of the plug. A rail structure, not shown, enables us to remove the upper parts of the plug and inner shield cylinder to provided access to the drift chamber electronics.

The machining, bending, welding and annealing were done at KHI. Some construction processes are shown in Figs. 17 and 18; the latter also shows the shield as it is being aligned, and mounted and aligned, with half of the cover plate remaining to be mounted.

5. The bucking coil and its power supply

The bucking coil is constrained in the space between the moveable backward end doors and the horsecollar, and at a radius beyond the support of the quartz bars. The aim of the design is to allow for as many ampere-turns as possible in this restricted region, approximately 100 mm in Z, and 220 mm in radius, starting at a radius of about 945 mm.

The bucking coil, designed and built at SLAC, is a conventional magnet, water-cooled, with 140 turns of square hollow core copper, 0.375 in. on a side, insulated with polyester glass fiber. The bucking coil power supply consists of two off-the-shelf 15 kW switcher power supplies connected in parallel, a thyristor reversing switch, a zero-flux current measuring transductor, and a controller/regulator connected to the PEP-II Bit-Bus power supply control network. It has a combined maximum rating of $\pm$ 300 A.

6. Design and construction of the DIRC mapper

The aim of the DIRC mapper is to measure the field components inside the shield at positions corresponding to the faces of the PMTs [10]. It was designed and built at the Budker Institute. It consists of a rigid support structure, mounted on the horsecollar, which can rotate about the beam axis. Three-dimensional probes are placed at three positions along the PMT rows, at the two extremes and in the middle.

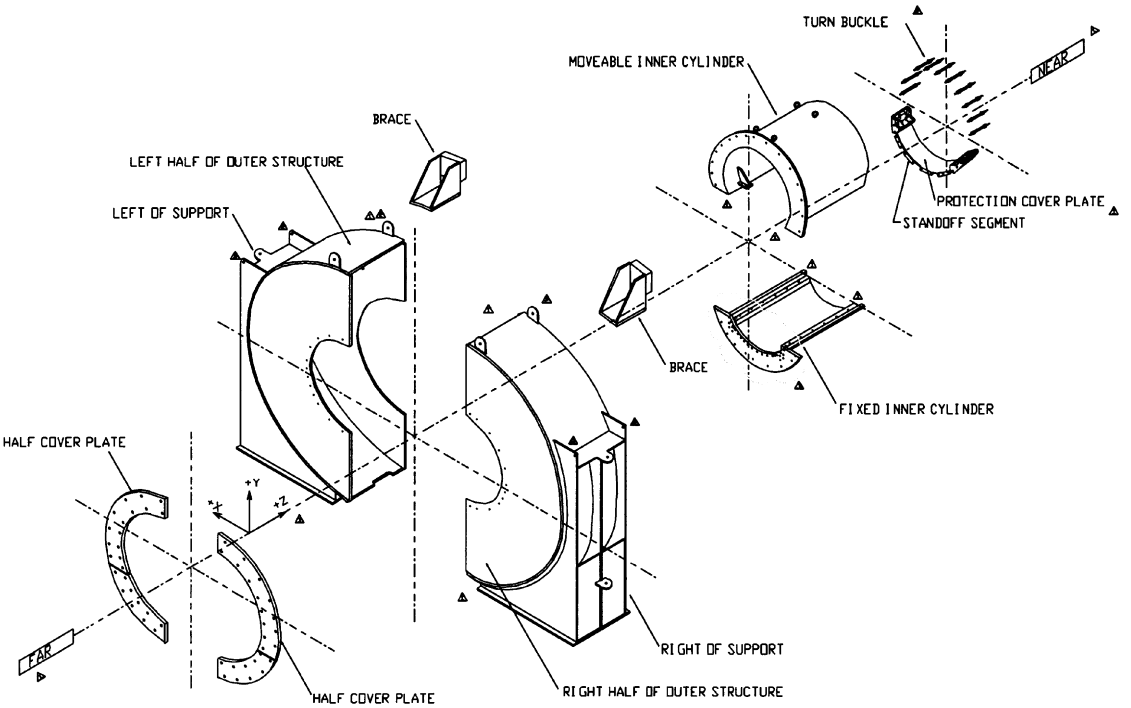

Fig. 16. Exploded isometric view of the DIRC shield design.

We will now describe the mechanics and the probes in some detail.

6.1. Mechanics

The mechanical design of the magnetic measurement system is shown in Figs. 19 and 20.

A rigid frame is attached to the platform moving around the circular rail mounted on the horsecollar. All elements, such as frame, removable platform and circular rail are fabricated from aluminum alloy. The movement of the platform along the rail is provided by three rollers. Three 3D probes are fixed on the arc of the frame.

The step motor mounted on the platform provides the motion of the frame. The motor has no permanent magnet inside. A worm gear is used to transfer the rotation momentum of the rotor.

The potentiometric method with the use of nichrome wire resistor of 0.8 mm diameter is used to measure the azimuthal angle ϕ. This wire is located in the groove on the rail. An electric contact attached to the platform moves along the rail together with the platform. The wire resistor is supplied by 100 mA current. The accuracy of the azimuthal angle measurement is about 0.2°.

6.2. Probes

Both ferro-probes (Magnetically Modulated Permalloy Probes or MMPP) and Hall probes are used. Each set of 3D probes consists of one 3D ferro-probe and one 3D Hall probe located next to each other. The sensitive volume of a set is a cube of $20 \times 20 \times 20$ mm^3. The locations of the 3D probes on the rigid frame correspond to the faces of the PMTs as shown in Fig. 19, with the definitions:

- #2 probe — furthest PMT from beam line,
- #1 probe — intermediary PMT,
- #0 probe — closest PMT to beam line.

The measurement coordinate system has 0° as the downward direction, rotating in the clockwise direction as viewed from the rear of BABAR.

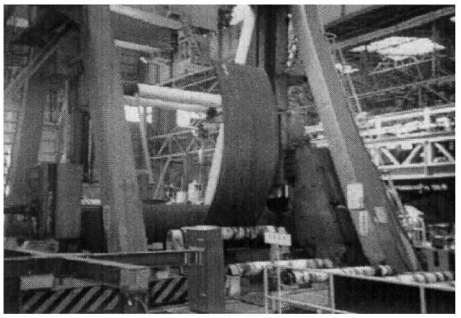

(a) Rolling of outer cylinder

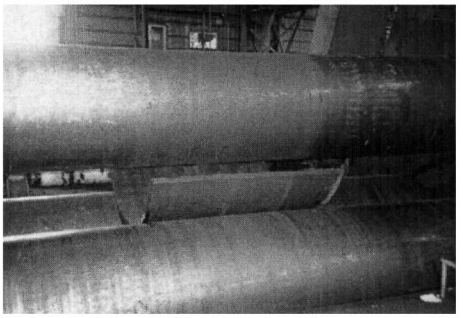

(b) Rolling of inner cylinder

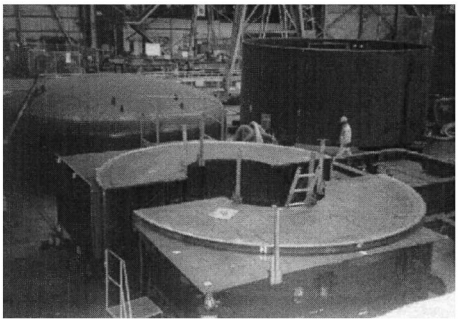

(c) Outer structure in two halves

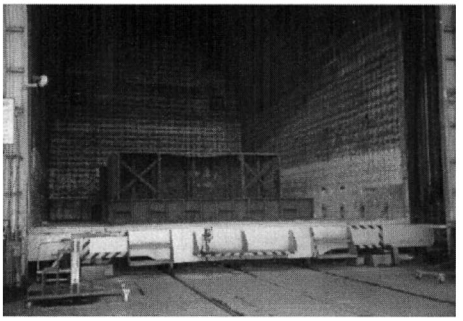

(d) Oven used to anneal each half

Fig. 17. Construction of the DIRC shield: I.

6.2.1. Ferro-probes

Ferro-probes are used to measure relatively low fields up to about 10 G. The ferro-probe is supplied with a measuring electronic unit which transforms magnetic field into voltage with a coefficient of about 0.5 V/G. Each 3D ferro-probe is arranged inside a cube of $10 \times 10 \times 10$ mm^3.

The design of one coordinate of a ferro-probe is shown in Fig. 21. It consists of a permalloy core of 20 μm diameter and 7 mm long located in the quartz tube. This core was annealed in advance and has a very small coercive force. The common excitation and compensation coils are wound along the quartz tube. The signal coil is wound at the middle of the tube. Rectangular 16 kHz impulses from a generator are applied to the excitation circuit. The signal in the signal coil is proportional to the B derivative in the core. The amplitude of the second harmonic ($2f = 32$ kHz) of this signal is proportional to the measured B_{ext}. An integrating ADC with a multiplexer is used to read out the probes with 14–20 bit resolution for two scales: 8 and 0.5 V. The long-term zero drift is less than 0.02 G within a 20–30°C temperature range.

6.2.2. Hall probes

Hall probes are used to measure relatively high fields exceeding 5 G, thus overlapping the ferro-probe sensitive region. One 3D set of Hall probes consists of three probes glued on the sides of an aluminum cube, $3 \times 3 \times 3$ mm^3. This unit is assembled in a box $9 \times 15 \times 62$ mm^3. The stabilized DC current source which is used to supply the Hall probes has a stability of 10^{-5}.

6.2.3. Probe calibration

A special calibration system is used to measure the zero offset and sensitivities of the probes. The calibration is performed with the help of Helmholtz coils located inside a zero-field box (less than 0.01 G) manufactured from annealed permalloy. It can produce magnetic fields up to 50 G. We used

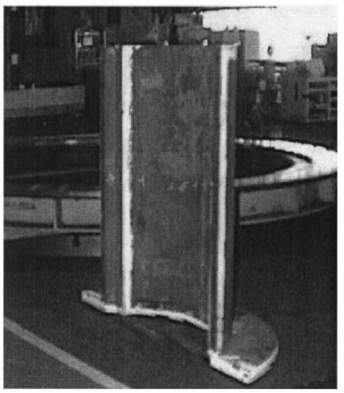

(a) Lower, or fixed, part of inner cylinder before shot-blasting in factory

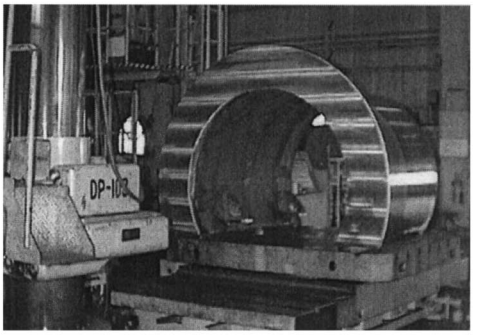

(b) Upper, or moveable, part of inner cylinder in machining

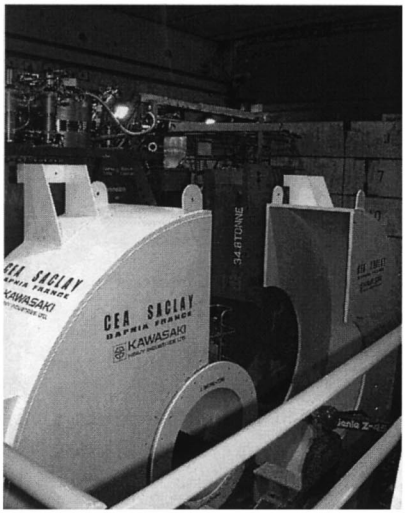

(c) Shield in process of being adjusted at *BaBar*

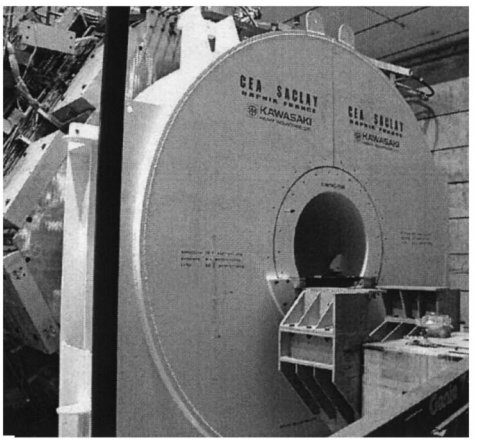

(d) Shield fully mounted at *BaBar*, except for the top of cover plate

Fig. 18. Construction of the DIRC shield: II.

a Hall probe calibrated by an NMR probe to measure the coefficient between the current and magnetic field of these coils. The estimated error is 0.1%.

6.3. On-line software for mapper

On-line code written in C++ runs under a Linux operating system on an IBM PC. We used a standard CAMAC interface PPI-2 and Crate Controller developed at the Budker Institute. This code allows one to drive the mechanics, calibrate the probes, measure the magnetic map and display the resulting curves during measurements.

7. Field mapper at backward quadrupoles

A single Hall probe was used, which could be oriented to measure any component. It was placed

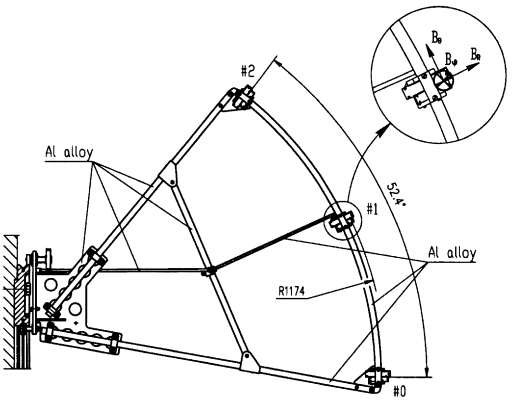

Fig. 19. Side view of the mechanism. The location of probes is at the PMT faces with #0 the closest to the beam and #2 the furthest.

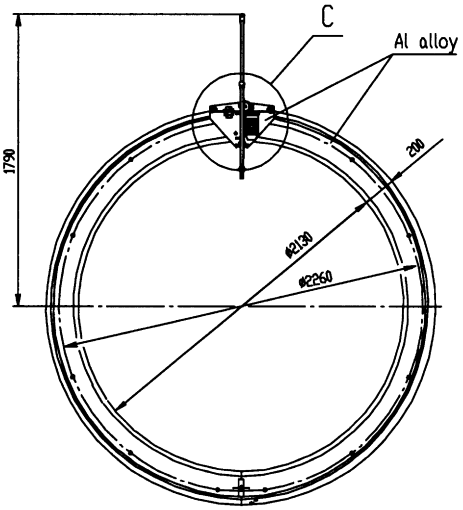

Fig. 20. Front view of the mechanism. The mechanism rotates azimuthally about the beam direction.

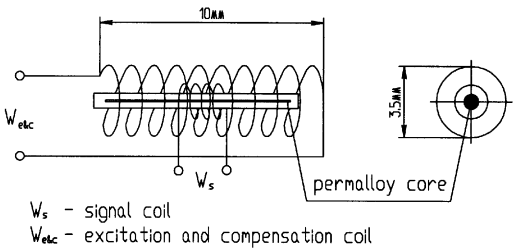

Fig. 21. Design of ferro-probe or MMPP (one coordinate).

in an aluminum channel, which had a 3 m scale graduated in mm. The channel was oriented on a line approximating either the LEB or HEB beam trajectory, or parallel to the beam axis at a radius = 25 cm.

8. Results of measurements

8.1. Gaussmeter measurements with no shield

The solenoid was commissioned before mounting the DIRC shield. Measurements were taken at that time with a hand-held gaussmeter to obtain an order of magnitude of the fringe field with and without the bucking coil turned on. The reproducibility of the method was about $\pm$ 10%. There was no coordination of the powering of the two coils.

With the bucking coil off or on, the results for the shield region are given in Table 1. They are valid for one azimuth and are difficult to compare to a 2D simulation. Note that the PMT closest (furthest) to the beam line is at $R = 83.7$ (186) cm and $Z = Z_h$-126 (68) cm.

The results for the Q2 region as a function of Z on a straight-line approximation to the LEB orbit are given in Fig. 22 and compared to the 2D Mermaid predictions. The results are quite accurate at the exit of the backward endcap as well as at

Table 1
Gaussmeter results for $B_{mod}(B_Z)$ with bucking coil OFF (ON) in the shield region. Z_h is the Z at the exit of the horsecollar. Solenoid current at 1.05 nominal = 4830 A (nominal = 4600 A)

OFF				
Radius (cm)	Z_h B_{mod}(G)	$Z_h - 80$ B_{mod}(G)	$Z_h - 160$ B_{mod}(G)	$Z_h - 290$ B_{mod}(G)
0	220	50	20	7
70	175	25	15	7
105	30	20	9	
ON				
Radius (cm)	Z_h B_Z(G)	$Z_h - 80$ B_Z(G)	$Z_h - 160$ B_Z(G)	$Z_h - 290$ B_Z(G)
0	− 2.8	− 0.2	− 2.9	− 2.6
70	—	− 2.2	− 3.1	− 2.6
105	− 7.6	− 3.5	− 3.6	− 2.8

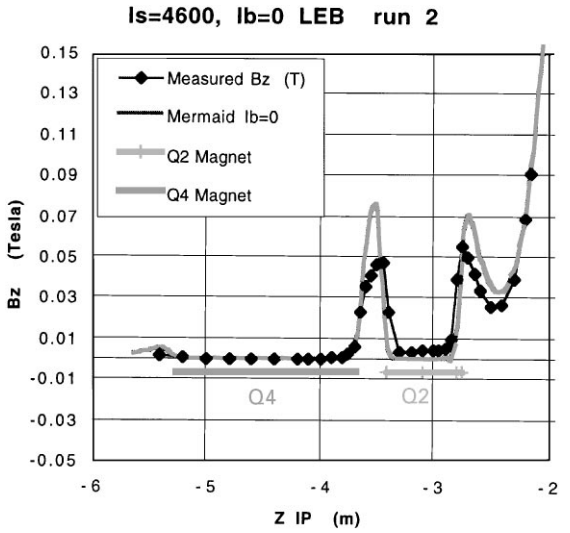

Fig. 22. Gaussmeter results for B_Z in the Q2 region with the bucking coil off. The 2D Mermaid predictions are also known. Note that Z refers to the distance from the interaction point.

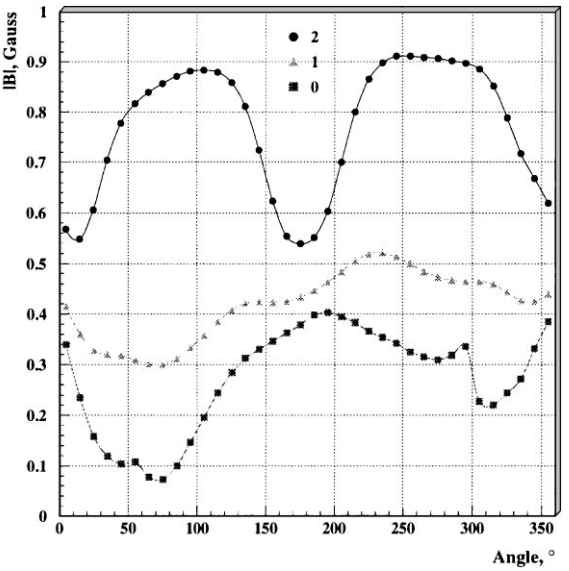

Fig. 23. B_{mod} vs. azimuthal angle with magnetized BABAR iron, only unmagnetized inner cylinder mounted and both coils turned off.

the quadrupoles, while differing by about 20 G at the mid-point between the quadrupoles. Note the large field at Q2 which the bucking coil must compensate.

8.2. Mapper measurements with "no" magnetization of the shield

8.2.1. No field and minimal shield

Fig. 23 shows the measurements reflecting the remnant field in the BABAR doors, horsecollar and skid plates. The maximum B_{mod} was about 0.90 G, and was observed for probe 2 about the horizontal direction (90° and 270°). For this probe, it was a minimum in the vertical direction, about 0.55 G. The maximum and minimum values are approximately left–right and up–down symmetric.

8.2.2. No field and full shield

The mounting of the shield greatly reduced the influence of the remnant field of BABAR doors at the PMT positions. More important, a very low measured field (less than 0.2 G) shown in Fig. 24 demonstrates that the iron used in the shield construction had a very low residual field.

8.2.3. Ramp to full field

The solenoid and bucking coils were ramped together in five steps to the nominal operating currents. Measurements were made at each step.

Inside the shield, the maximum $B_{\perp}$ was observed for probe 0 at around 60°. At the nominal currents, the maximum perpendicular component of the field at the PMTs is 0.8 G, quite reasonable for PMT operation. The fringe field is not linear (see Fig. 25) in that the BABAR iron is not saturated at low currents; at these currents, the bucking coil over-compensates the solenoid; It should also be noted that in simulations, a linear relationship between the ramping of the two coils leads to fields in the shield iron of about 1 kG at about mid-ramp, while an optimum relationship gives a maximum field of about 0.5 kG at the final, or nominal current. Therefore, a linear ramping function will lead to some extra magnetization of the iron.

Fig. 26 shows the measurements along the LEB trajectory in the vicinity of Q2. Note the same effect of over-compensation due to the bucking coil before the iron becomes saturated.

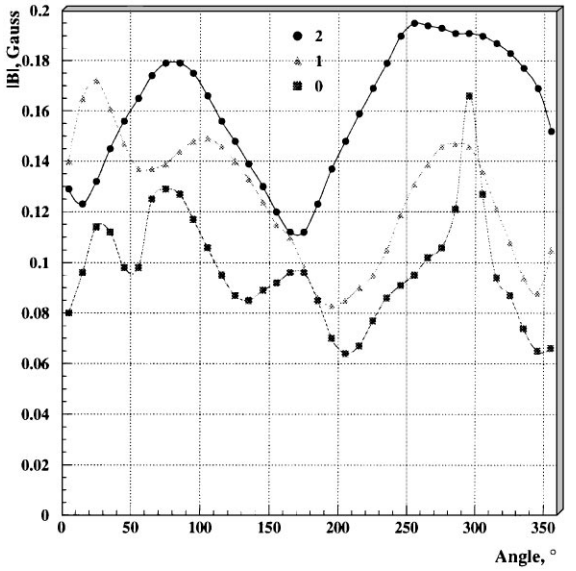

Fig. 24. B_{mod} vs. azimuthal angle with magnetized BABAR iron, completed unmagnetized shield and both coils turned off.

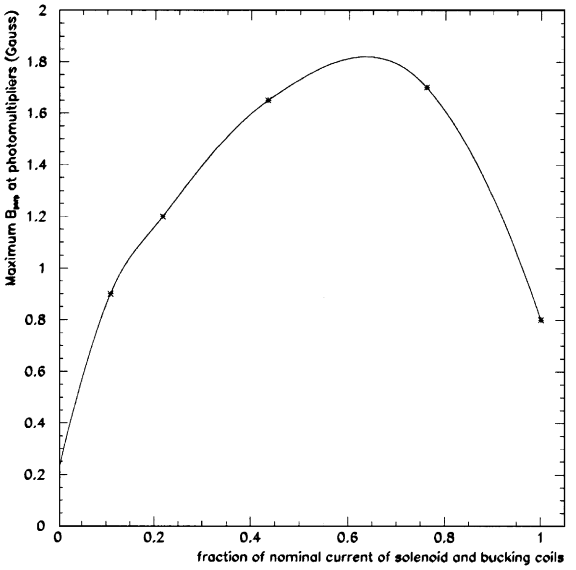

Fig. 25. Maximum $B_{\perp}$ vs. fraction of nominal operation current for both coils, ramped together.

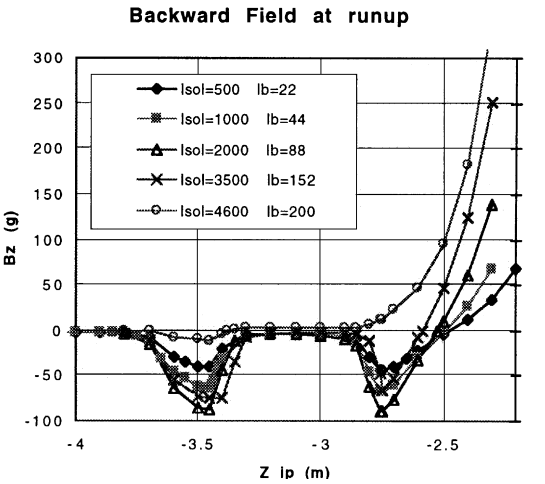

Fig. 26. Results at Q2 as the solenoid and bucking coils were ramped together. Note that Z refers to the distance from the interaction point.

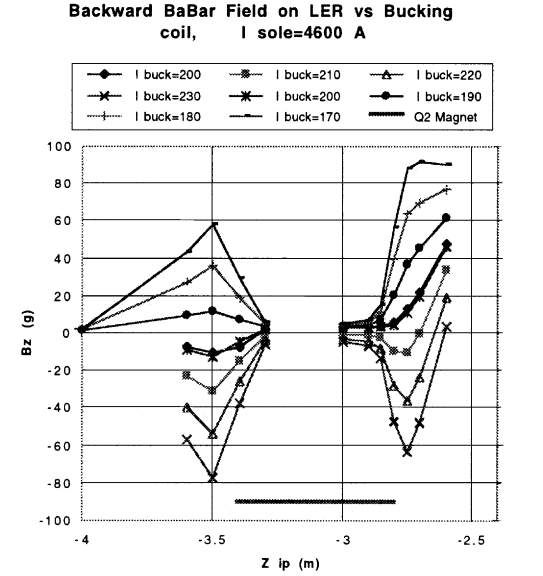

Fig. 27. Results at Q2 as the bucking coil current was varied, while the solenoid was at nominal field. Note that Z refers to the distance from the interaction point.

8.2.4. *Optimization of the bucking coil current*

The bucking coil current was varied to determine the optimum currents for PMT and quadrupole operation. It was increased to 230 in 10 A steps and then was reduced back to 200 A. The current was then reduced to 170 in 10 A steps.

Fig. 27 shows the measurements along the LEB trajectory in the vicinity of Q2. It is clear that the optimum is near 200 A. Note that this current

is about 10% lower than the prediction (Section 3.2). For the optimal current, a fine Z scan was performed along the LEB direction from the exit of the backward end cap to beyond Q4; see Fig. 28 for the measurements. The 2D Mermaid results are also shown; they differ by less than about 5 G at and between the quadrupoles, and track quite well near the doors where B_Z rises rapidly.

For the PMTs, the value of $B_\perp$, measured at $\approx 60^\circ$ (the maximum point), differed in the two 200 A measurements due to hysteresis effects; it was *reduced* from 0.8 to 0.6 G. At the 170 A, the three probes had the same maximum value, 0.5 G which is the optimum for the PMTs. This value is about 15% lower than at 200 A, the value that was determined as optimum for Q2, in good agreement with the calculation (Section 3.2). The bucking coil current was cycled back to 200 A as follows: 170 A → 230 A → 180 A → 220 A → 190 A → 210 A → 200 A at which point we observed a reduction in the hysteresis. See Fig. 29 for the scan at the last current. The maximum $B_\perp$ is about 0.8 G and a left–right asymmetry is observed, probably due to residual shield magnetization. (No effects of shield magnetization were observed at Q2.)

8.3. Mapper measurements with magnetization of shield

A magnetization of the shield was induced by ramping the bucking coil to zero, while the solenoid remained at its nominal value. The maximum $B_\perp$ was now over 5 G, demonstrating the necessity of the bucking coil. See Fig. 30. This maximum point was at an angle $\approx 300^\circ$ and another local maximum was observed at $\approx 60^\circ$; it is notable that these angles correspond to the horizontal gaps in the cover plates.

The bucking coil was now ramped back up to 200 A, and the maximum $B_\perp$ was reduced to about 2.1 G, as can be seen in Fig. 31. This maximum value corresponds to the limit set for the PMTs, see (2.1), but leaves little margin. Since we want a more robust solution, we have investigated different demagnetization schemes.

8.4. Demagnetization

A typical demagnetization cycle is shown in Fig. 12, requiring a current reversal, e.g. when the solenoid is off, but it is also possible to use a demagnetization cycle about a finite current, e.g. when the solenoid is on.

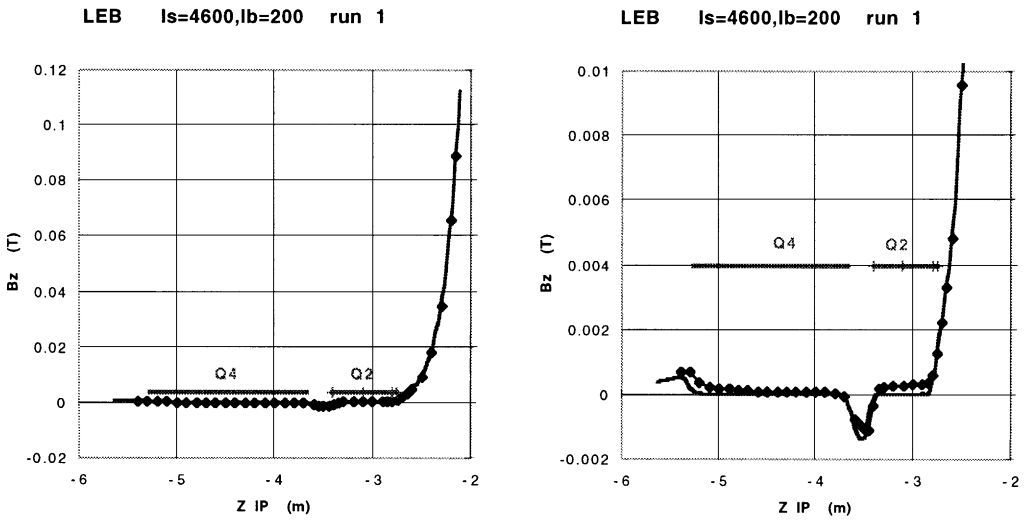

Fig. 28. Fine scan in Z at Q2 at the optimum bucking coil current with two scales. The 2D Mermaid prediction with $I_b = 220$ A is also shown. Note that Z refers to the distance from the interaction point.

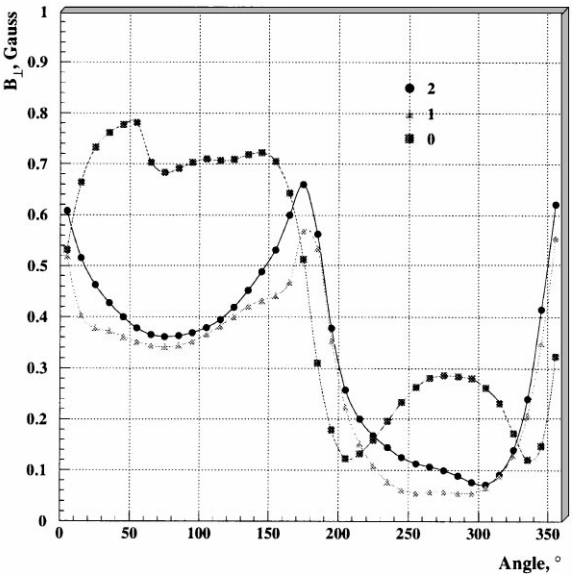

Fig. 29. $B_{\perp}$ vs. azimuthal angle with the solenoid at its nominal current and the bucking coil at the optimum current for Q2.

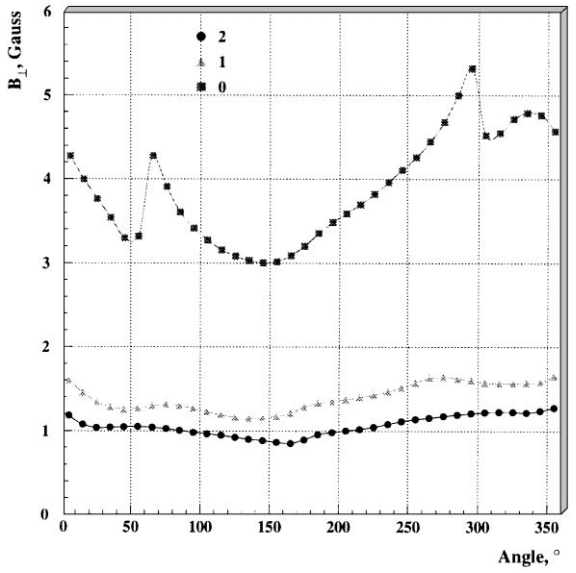

Fig. 30. $B_{\perp}$ vs. azimuthal angle with the solenoid at its nominal current and the bucking coil turned off to induce magnetization in the shield iron.

A first incomplete demagnetization was performed by varying the bucking coil current around 200 A with the following cycle: 200 A → 250 A → 155 A → 240 A → 165 A → 230 A → 175 A → 220 A → 185 A → 210 A → 195 A → 200 A, each step performed in 2 minutes. While the shape was unchanged, the 2.1 G peak seen in Fig. 31 was reduced to 1.15 G (to be compared to 0.8 G for the unmagnetized case). This already demonstrated that demagnetization using the bucking coil was feasible.

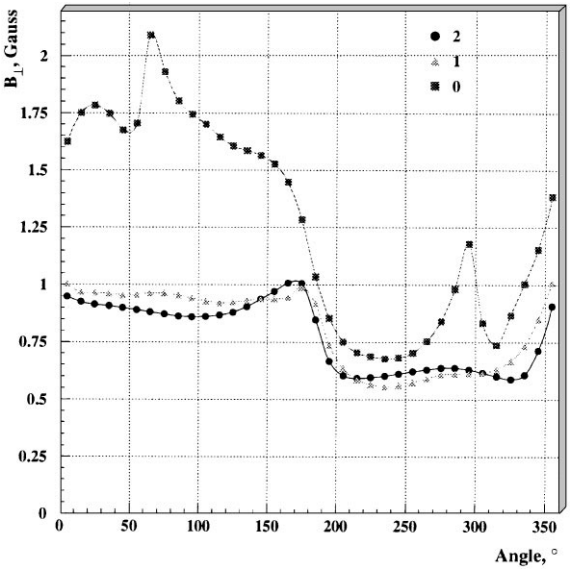

Fig. 31. $B_{\perp}$ vs. azimuthal angle with the solenoid at its nominal current and the bucking coil at 200 A after the magnetization of the shield iron.

8.4.1. Solenoid "crash"

When the solenoid was discharged rapidly from full current (38 s time constant), the bucking coil power supply could not track, and the shield was re-magnetized. A demagnetization cycle of the bucking coil current around 0 A was attempted as follows: 0 A → −200 A → 190 A → −180 A → 170 A → −160 A → 150 A → −140 A → 130 A → −120 A → 110 A → −100 A → 90 A → −80 A → 70 A → −60 A → 50 A → −40 A → 30 A → −20 A → 0 A, each step performed in 2 min, and the result is shown in Fig. 32. The maximum $B_{\perp}$ is 0.22 G which is close to the one before the shield was put in a magnetic field (Fig. 24); we plan to use this scheme for demagnetization when the solenoid is off.

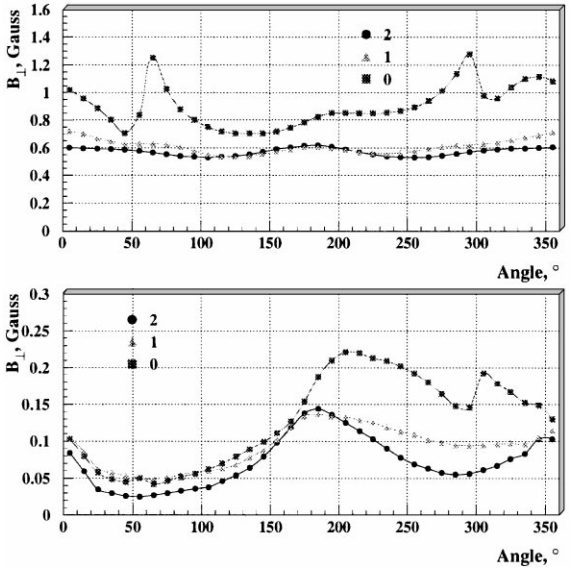

Fig. 32. Comparison of $B_\perp$ vs. azimuthal angle after solenoid "crash" and after a demagnetization cycle of the bucking coil around 0 A. Both coils are off.

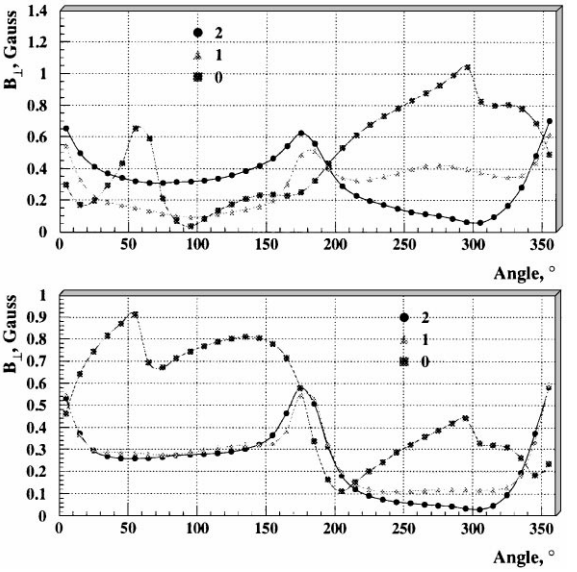

Fig. 33. Comparison of $B_\perp$ vs. azimuthal angle after a bucking coil "crash" and after a demagnetization cycle of the bucking coil around 200 A with the solenoid at full current. Both coils are on.

8.4.2. Bucking coil "crash"

While ramping up both power supplies, a problem caused the solenoid to be discharged rapidly again, and the shield was re-magnetized. The two power supplies were ramped up once again, and with the solenoid at full current, demagnetization was attempted with a cycle around 200 A as follows: 200 A → 300 A → 105 A → 290 A → 115 A → 280 A → 125 A → 270 A → 135 A → 260 A → 145 A → 250 A → 155 A → 240 A → 165 A → 230 A → 175 A → 220 A → 185 A → 210 A → 195 A → 200 A, each step performed in 2 min. The result is shown in Fig. 33, and should be compared to Fig. 29. The maximum value is now 0.9 G, quite comparable to the 0.8 G previously attained.

While this scheme is satisfactory, it could possibly reduce the "on-time" of the experiment. Therefore, for a bucking coil "crash", another method of demagnetization was developed. We compensated for the magnetization by raising the bucking coil to a current above 200 A, called the overshoot current, and then lowering the current to the nominal 200 A current. We found that this was not only possible, but optimum in that the apparent BABAR left–right asymmetry could be compensated.

Table 2
Operation of the overshoot current, I_{over}

I_{over}	max B_{perp}, left side	max B_{perp}, right side
200	1.9	1.2
250	0.68	0.56
260	0.61	0.61
275	0.58	0.72
300	0.54	0.88

In Table 2, we show the results of the optimization. Each I_{over} was obtained starting at a null bucking coil current.

In Fig. 34 we see the left–right compensation around the optimum value of $I_{over} = 260$ A. This result is in relatively good agreement with the calculation (Fig. 11) though some residual field probably still influences the probe 0 result. Nonetheless, the results for probes 0 and 2 have about the same maximum value. In the experiment, we shall use this demagnetization scheme when the solenoid is at its nominal current.

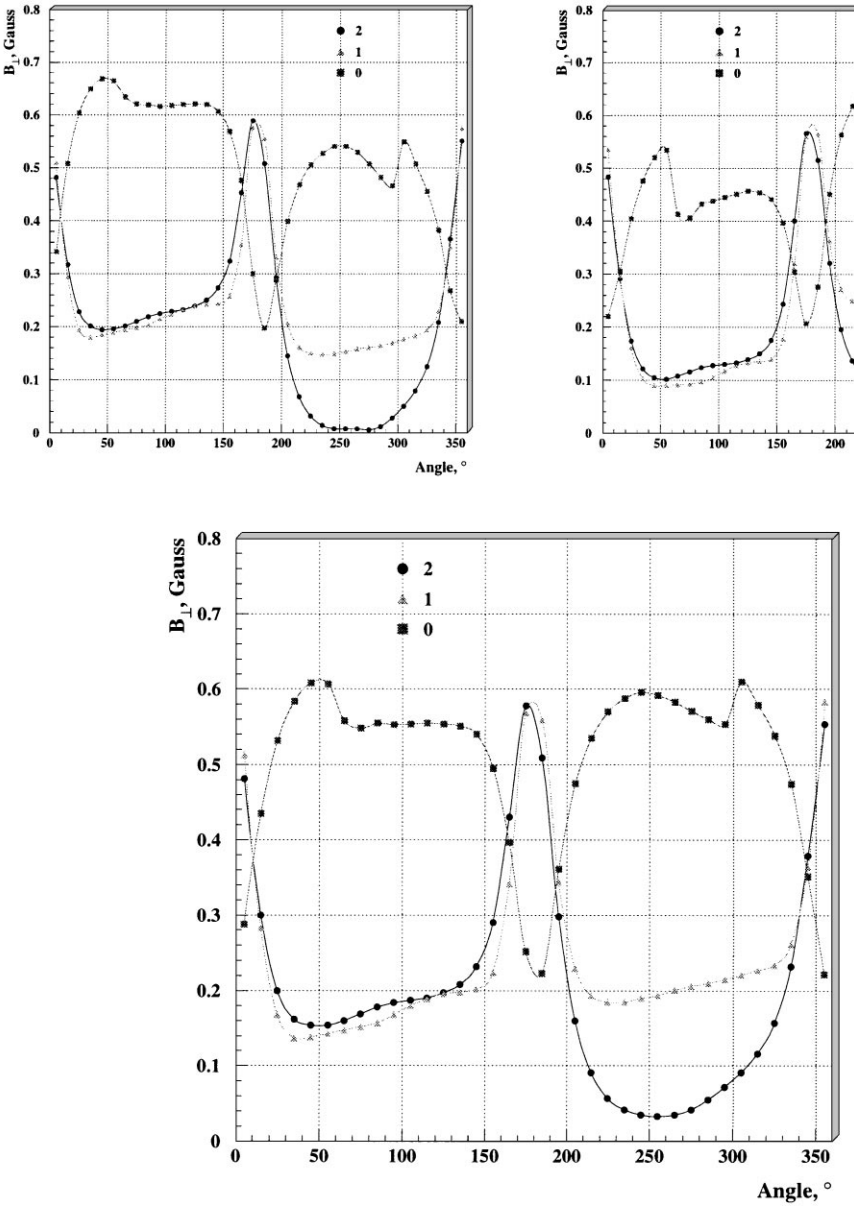

Fig. 34. Comparison of $B_\perp$ vs. azimuthal angle for the overshoot currents = 250 and 275 A, and the optimum current, 260 A.

Starting with a maximum $B_\perp$ of about 2 G when one of the two coils is inoperative and then is ramped up, the measurements with the simple demagnetization scheme show that a maximum $B_\perp = 0.6$ G can be attained, in good agreement with the predictions, see Section 3.4. This maximum field is quite robust for good PMT operation.

9. Conclusions

We have obtained low fringe fields in the backward part of the BABAR detector by using a bucking coil in conjunction with a very pure iron shield.

For the PMT region, within the shield, the measurements are in the sub-Gauss region, and

a precise quantitative comparison with the simulation is masked somewhat by the magnetization of the shield which is difficult to avoid. As we have seen, this magnetization has a complicated azimuthal dependence.

For the quadrupole region, a more quantitative comparison can be made between the measurements and the 2D axisymmetric Mermaid model as shown in Fig. 28. The results are quite accurate at the exit of the backward endcap where the steep fall-off is very well reproduced, even in the blown-up scale. Differences of the order of less than 5 G are seen at and between the quadrupoles.

The field in the PMT region is less than 1 G, in good agreement with the calculation. A simple method of demagnetization has been found, with a maximum $B_{\perp} = 0.6$ G in the PMT region. Demagnetization procedures have been investigated successfully and have become semi-automatic.

Acknowledgements

The authors are grateful for support by the Direction des Sciences de la Matière (CEA, France), SLAC and Budker Institute of Nuclear Physics (Novosibirsk). They would like to thank the solenoid/cryogenic group led by T. O'Connor and R. Burgess, the installation group led by B.L. Byers, and O. Fackler for his initial work on this subject.

The Saclay group would like to thank Kawasaki Heavy Industries, in particular Mr. Inoue and Mr. Numasawa, for their efficient and agreeable collaboration on this project; in addition, the authors would like to thank KHI for its permission to use Figs. 5, 17 and 18.

One of the authors (GL) would like to thank J.-M. Baze for his initiation and help with Castem 2000. The Novosibirsk group would like to thank A. Dubrovin for his help with Mermaid.

References

[1] An Asymmetric B Factory Based on PEP: Conceptual Design Report, SLAC-REP-91-372, 1991.
[2] The BABAR collaboration, Technical Design Report, SLAC-REP-95-457, 1995.
[3] H. Staengle et al., Nucl. Instr. and Meth. A 397 (1997) 261.
[4] Ph. Bourgeois et al., DIRC note 53, 1996, in particular, Figs. 7 and 8.
[5] J. Osborn, J. Tanabe, D. Yee, F. Younger, Design of the PEP-II interaction region septum quadrupole, 97 Particle Accelerator Conference, Vancouver, BC, Canada, 12–16 May 1997.
[6] P. Verpaux, T. Charras, A. Millard, Castem 2000, une approche moderne du calcul des structures, in: J.M. Fouet, P. Ladeveze, R. Ohayon (Eds.), Calcul des Structures et Intelligences Artificielle, Pluralis, 1998, pp. 261–271.
[7] Mermaid User's Guide, Novosibirsk, 1994.
[8] Kawasaki Heavy Industries, private communication.
[9] E. Antokhin et al., BABAR note 344, 1996.
[10] A. Buzykaev et al., DIRC note 101, 1998.